RSC Sustainability

ROYAL SOCIETY OF CHEMISTRY

PAPER

View Article Online
View Journal | View Issue

Cite this: *RSC Sustainability*, 2025, **3**, 5556

Unveiling the synergistic potential of $LaMnO_3$–CeO_2 composites in supercapacitor applications

Alisha Dhakal, *[a] Felio Perez[b] and Sanjay R. Mishra*[a]

Received 4th September 2025
Accepted 14th October 2025

DOI: 10.1039/d5su00726g

rsc.li/rscsus

This study investigates the synthesis of $LaMnO_3$–CeO_2 composites with varying CeO_2 contents ((100 − *x*)% $LaMnO_3$–*x*% CeO_2; *x* = 0, 10, 30, 50, 100 wt%) *via* an autocombustion method to elucidate their synergistic electrochemical properties. X-ray diffraction (XRD) confirmed the presence of both $LaMnO_3$ (LMO) and CeO_2 phases in the anticipated stoichiometric ratios. Nitrogen adsorption–desorption isotherms revealed a mesoporous structure, with the LMO–CeO_2 (70 : 30) composite exhibiting the highest specific surface area of 14.32 $m^2\ g^{-1}$, as determined by the Brunauer–Emmett–Teller (BET) method. X-ray photoelectron spectroscopy (XPS) provided insights into the ion valences and chemical composition of the composites. Electrochemical performance was evaluated in a 1 M KOH aqueous electrolyte using a three-electrode configuration. The LMO–CeO_2 (70 : 30) composite demonstrated superior performance, achieving a specific capacitance of 830.3 F g^{-1} at a scan rate of 1 mV s^{-1} and 637.6 F g^{-1} at a current density of 1 A g^{-1}, corresponding to an energy density of 31.9 Wh kg^{-1} at a power density of 357.5 W kg^{-1}. These results underscore the synergistic enhancement of electrochemical properties through the integration of $LaMnO_3$ and CeO_2, offering significant potential for the development of high-performance materials for energy storage applications.

Sustainability spotlight

The growing need for sustainable energy storage requires materials that are efficient, affordable, and environmentally friendly. In this work, we introduce $LaMnO_3$–CeO_2 composites as electrode materials for supercapacitors, synthesized by a simple and scalable autocombustion process. These oxides are composed of earth-abundant elements, avoiding the use of costly or scarce metals. By tuning the $LaMnO_3$–CeO_2 ratio, the composites show enhanced charge storage and long-term stability, offering a pathway to durable devices with reduced material waste. This research supports global efforts toward clean, sustainable energy storage solutions.

Introduction

The demand for power and energy resources is increasing due to the rapid population growth and industrialization's fast-paced development.[1] Supercapacitors offer several benefits, including high power density, remarkable cycling stability, and quick charging and discharging rates, in contrast to conventional batteries, which store energy through chemical reactions.[2–6] ABO_3 perovskite materials have recently garnered significant attention as potential replacements for traditional metal oxides in electrochemical applications. The key feature of ABO_3-type perovskites, such as $LaMnO_3$, is their ability to undergo redox reactions, which lead to pseudocapacitance. The Mn^{3+}/Mn^{4+} redox couple governs the redox behavior in $LaMnO_3$. During charge/discharge cycles, Mn can switch between these oxidation states, contributing to the material's overall capacitance. This faradaic charge storage mechanism (pseudocapacitance) significantly enhances the energy density of the supercapacitor, which is one of the primary performance metrics of the capacitor. However, for redox reactions to occur efficiently, electrons must move between the Mn ions and the external circuit. Low conductivity hinders the movement of these electrons, which limits the efficiency of the pseudocapacitive charge storage and reduces the overall capacitance. Additionally, at higher current densities (faster charge/discharge), the high conductivity of a material is desirable to effectively engage redox couples during the cycle. This enhances charge transfer kinetics, minimizes internal resistance, and reduces voltage losses. One approach to improving the supercapacitor performance of $LaMnO_3$ is to combine it with conductive materials such as graphene,[7] carbon nanotubes,[8] or conducting polymers,[9] thereby forming $LaMnO_3$ composites. In addition to conductivity mismatch, the structural mismatch between $LaMnO_3$ and graphene, for example, could cause the loss of contact between the two components, leading to poor charge/discharge performance.

The above issue is addressed by combining $LaMnO_3$ with similar oxides, forming a compatible interface with $LaMnO_3$.

[a]*Department of Physics and Materials Science, The University of Memphis, Memphis, TN 38152, USA. E-mail: srmishra@memphis.edu; adhakal@memphis.edu*

[b]*Integrated Microscopy Center, The University of Memphis, Memphis, TN 38152, USA*

Along with reducing strain and facilitating better electron transport between the oxides, the oxide's pseudocapacitive behavior can lead to a synergistic effect, improving the total capacitance of the supercapacitor. For example, $LaMnO_3$@NiO composites were synthesized by A. Arya *et al. via* a hydrothermal method assisted by sol–gel processing. They claimed the C_{SP} of 170 F g^{-1} when measured at 10 mV s^{-1}.[10] P. M. Shafi *et al.* synthesized $LaMnO_3/Mn_3O_4$ composites using a one-pot synthesis method. The C_{SP} of 135 F g^{-1} was achieved at 1 A g^{-1} in 1 M Na_2SO_4 solution, corresponding to an energy density of 75 Wh kg^{-1} and a power density of 1000 W kg^{-1}.[11] $LaMnO_3$–MnO nanoarrays supported by carbon cloth were synthesized through one-step electrodeposition by P. Ma *et al.* These nanoarrays demonstrated a C_{SP} of 260 F g^{-1} in a 0.5 M Na_2SO_4 at 0.5 A g^{-1}.[12] $LaMnO_3$@$NiCo_2O_4$ nanoarchitecture in Ni foam was synthesized by H. Tian *et al.* using the hydrothermal route, which exhibited a C_{SP} of 811 F g^{-1} in 6 M KOH and at 1 A g^{-1}.[13]

Considering its structural compatibility, CeO_2 is a promising choice for forming a composite structure with $LaMnO_3$. While $LaMnO_3$ has a perovskite structure, CeO_2 adopts a fluorite structure; however, both exhibit cubic symmetry, making them structurally compatible at the interface. While $LaMnO_3$ provides efficient electron transport *via* hopping through Mn–O–Mn bonds, CeO_2 provides oxygen vacancies for ionic transport. These two conductivity mechanisms combine at the interface, creating a simultaneous pathway for both electronic and ionic charge transport. Furthermore, Mn^{3+}/Mn^{4+} redox transitions in $LaMnO_3$ could be coupled with Ce^{4+}/Ce^{3+} redox transitions in CeO_2,[14] promote electron exchange with multiple redox processes and thus enhance pseudocapacitance. Meanwhile, oxygen ions from $LaMnO_3$'s lattice can migrate into vacancies in CeO_2 and *vice versa*, and this movement could stabilize oxygen vacancies at the interface, increasing active sites for redox reactions. In fact, CeO_2 is known for its electrochemical stability in a wide range of electrolytes (both aqueous and organic), and it can withstand multiple charge/discharge cycles without significant degradation. This property enhances the cycling life of $LaMnO_3$–CeO_2 composites in supercapacitors.

This study presents a detailed electrochemical analysis of $LaMnO_3$–CeO_2 composites prepared *via* autocombustion. The process involves igniting a precursor mixture containing metal salts and fuels (such as urea or citric acid). When ignited, the heat generated by the combustion reaction leads to the rapid formation of highly porous and high surface area nanocrystalline particles.[15] As discussed above, the choice of $LaMnO_3$ as a composite component is due to its excellent redox activity, structural stability, and high theoretical C_{SP}. At the same time, CeO_2 has a highly reversible Ce^{3+}/Ce^{4+} redox transition, which is essential for its pseudocapacitive behavior. CeO_2 can easily switch between the +3 and +4 oxidation states in redox, allowing it to store and release charge through fast and reversible electron transfers. The choice further extends to CeO_2 as other rare-earth oxides, such as La_2O_3, Pr_2O_3, and Nd_2O_3, typically have more stable oxidation states (*e.g.*, La^{3+}, Pr^{3+}, Nd^{3+}) and do not exhibit the same level of redox versatility as CeO_2. Thus, enhanced electrochemical performance in $LaMnO_3$–CeO_2 composite is anticipated from the synergistic interactions across their interfaces, enabling simultaneous ionic and electronic transport. The nanoscale interface is expected to maximize the active area, shorten diffusion paths, and enhance charge separation, ensuring efficient charge storage with enhanced electrochemical performance.

Experimental section

Materials

The composites of $LaMnO_2$–CeO_2 were prepared using lanthanum(III) nitrate hexahydrate (La-nitrate, $La(NO_3)_3\cdot 6H_2O$), cerium(III) nitrate hexahydrate (Ce-nitrate, $Ce(NO_3)_3\cdot 6H_2O$), manganese(II) nitrate tetrahydrate (Mn-nitrate, $Mn(NO_3)_2\cdot 4H_2O$), and citric acid monohydrate ($C_6H_8O_7\cdot H_2O$). All chemicals were purchased from Sigma-Aldrich, USA, and used without purification.

Preparation of $LaMnO_3$–CeO_2 composites

Composites of $LaMnO_3$–CeO_2 were synthesized *via* the autocombustion process.[16] The weight% of $LaMnO_3$ and CeO_2 in the composite was adjusted according to the expression $(100 - x)$% $LaMnO_3$–x% CeO_2 (x wt% = 0, 10, 30, 50, and 100), and the resulting samples were designated as LMO, LMO–CeO_2 (90% : 10%), LMO–CeO_2 (70% : 30%), LMO–CeO_2 (50% : 50%), and CeO_2, respectively. Initially, the hydrous powders of La-nitrate, Mn-nitrate, and citric acid monohydrate were mixed in 20 mL of deionized (DI) water and stirred magnetically (solution-1). In a separate beaker, Ce-nitrate and citric acid monohydrate were dissolved in 20 mL of DI water and stirred for 20 minutes to ensure uniformity (solution-2). Subsequently, solution 2 was added to solution 1, and the mixture was heated at 120 °C with continued magnetic stirring until autoignition occurred. The resulting black powder was transferred to a crucible and calcined at 900 °C overnight in the furnace to yield $LaMnO_3$–CeO_2 composites. The chemical reaction in forming $LaMnO_3$–CeO_2 composites is presented as eqn (1), while Fig. 1 illustrates a schematic diagram of the synthesis process.

$$\begin{aligned} La(NO_3)_3\cdot 6H_2O + Ce(NO_3)_3\cdot 6H_2O \\ + Mn(NO_3)_2\cdot 4H_2O + C_6H_8O_7\cdot H_2O \\ \rightarrow LaMnO_3(\text{powder}) + CeO_2(\text{powder}) \\ + 8N_2\uparrow + 6CO_2\uparrow + 21H_2O + 5O_2\uparrow \end{aligned} \quad (1)$$

Electrode fabrication

Electrode fabrication was carried out according to previous work.[17] A 2 cm × 1 cm nickel foam (Ni-foam) was used for electrode preparation. It was first ultrasonicated for 10 minutes in 25 mL of 37% HCl solution and then rinsed with deionized (DI) water. Subsequently, it underwent another 10 minutes of ultrasonication in DI water and ethanol. Finally, after an additional 10 minutes of ultrasonication in ethanol, the samples were dried at 110 °C for 2 hours under vacuum conditions. To prepare the homogeneous electrode solution, 6 mg of the synthesized $LaMnO_3$–CeO_2 composite was stirred for 6 hours (magnetically) with 1 mg of polyvinylidene fluoride in 0.001 L of

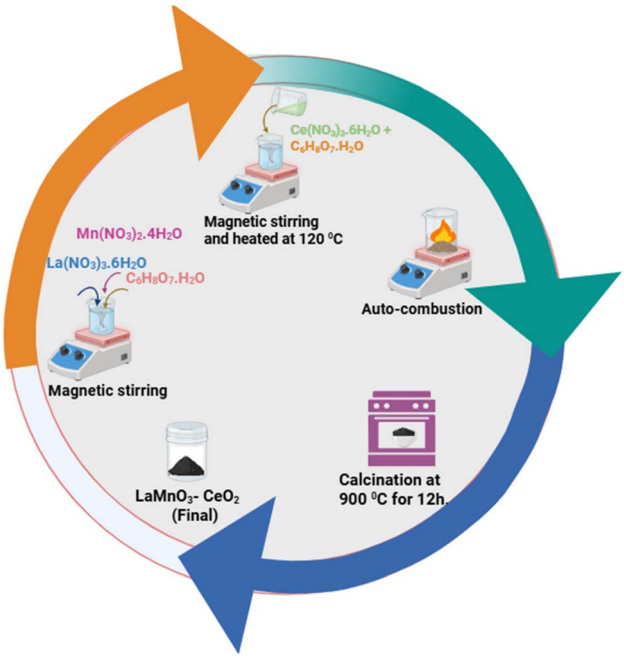

Fig. 1 A schematic of the autocombustion synthesis process of $LaMnO_3$–CeO_2 composites. Created with https://BioRender.com.

N-methylpyrrolidone to ensure uniform dispersion. After that, 0.6 mL of the resulting suspension was then deposited onto a 1 cm × 1 cm section of precleaned Ni-foam. The coated substrate was heated at 110 °C in a vacuum furnace for 20 hours. The loading of the active material was calculated by measuring the mass difference between the coated and uncoated Ni-foam.

Material characterization

The structural characteristics, including crystallographic phase and lattice parameters of the $LaMnO_3$–CeO_2 composites, were analyzed by using X-ray diffraction (XRD) using Cu Kα1 radiation of wavelength $\lambda \sim 1.5406$ Å on a D8 Advance diffractometer (Bruker, Germany). Data were collected using a Vantec solid-state detector (Bruker) with a 2θ range of 20°–70°, a step interval of 0.0484°, and a collection time of 0.2 s per step. Morphological analysis was performed using a Hitachi S-470 field-emission scanning electron microscope (FESEM) operated at 10 μA emission current and 20 kV as an acceleration voltage. With the help of energy-dispersive X-ray spectroscopy (EDX) using the Bruker Esprit spectrum 2.3, the elemental composition was determined. X-ray photoelectron spectroscopy (XPS) was performed using a Thermo Scientific K-Alpha system at a 0.1 eV step size to determine the binding energies, elemental compositions, chemical states, and electron configuration of the $LaMnO_3$–CeO_2 composite. The Brunauer–Emmett–Teller (BET) specific surface area and pore size distribution were determined using a NOVAtouch surface area analyzer (Quantachrome Instruments, USA) at 77 K, employing nitrogen adsorption. A Gamry instrument (Interface 1000, USA) with a three-electrode setup was used to perform the electrochemical measurements in 1 M KOH electrolyte. A stoichiometric quantity of KOH flakes was dissolved in 25 mL of deionized water to make a 1 M KOH. A platinum plate and Ag/AgCl were used as the counter and reference electrodes, respectively. A working electrode was fabricated by coating the sample onto a pure nickel foam substrate (area: 1 cm × 1 cm). The electrochemical performance was evaluated at room temperature using electrochemical impedance spectroscopy (EIS), cyclic voltammetry (CV), and charge–discharge measurements.

Results and discussion

Structure and morphology study

The XRD spectra along with the corresponding Rietveld refinement profiles of $LaMnO_3$–CeO_2 composites are shown in Fig. 2. The diffraction peaks observed at 2θ = 28.7, 33.2, 47.7, 56.6, 59.3, and 69.7° match the PDF number 01-073-6318, confirming the presence of CeO_2 with a face-centered cubic structure (space group *Fm*3*m*). Additionally, the primary peaks at 2θ = 22.9, 32.5, 32.8, 40.2, 46.9, 52.6, 58.2, and 68.1°

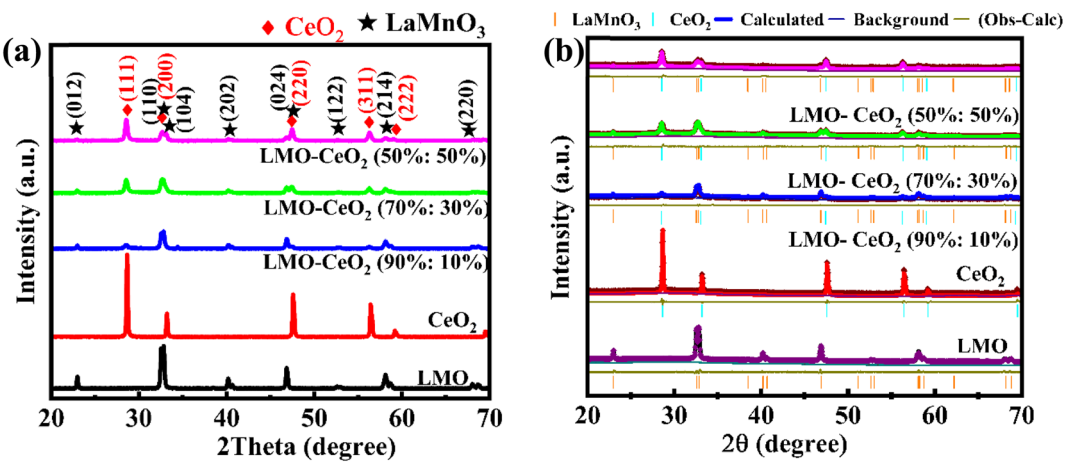

Fig. 2 (a) X-ray diffraction profiles and (b) corresponding Rietveld refinement results for the synthesized $LaMnO_3$–CeO_2 composites.

Table 1 Estimated composition of $LaMnO_3$–CeO_2 composites, lattice parameters, crystallite size, and microstrain derived from XRD data

		Lattice parameters						Crystallite size (nm)		Microstrain (10^{-3})	
		LMO			CeO_2						
Composites	Estimated composition	a (Å)	c (Å)	V (Å^3)	a (Å)	V (Å^3)		LMO	CeO_2	LMO	CeO_2
LMO	LMO	5.5027 (4)	13.3134 (6)	349.123 (23)	—	—		86.65 ± 0.03	—	1.6	—
CeO_2	CeO_2	—	—	—	5.40970 (8)	158.314 (7)		—	81.56 ± 0.05	—	1.3
LMO–CeO_2 (90% : 10%)	91.0% : 9.0%	5.5078 (8)	13.3371 (12)	350.39 (5)	5.4256 (13)	159.72 (11)		60.28 ± 0.04	29.50 ± 0.48	1.8	1.6
LMO–CeO_2 (70% : 30%)	68.0% : 32.0%	5.5054 (11)	13.3528 (24)	350.49 (8)	5.4231 (5)	159.49 (4)		33.01 ± 0.10	20.09 ± 1.38	1.2	0.1
LMO–CeO_2 (50% : 50%)	50.5% : 49.5%	5.5063 (26)	13.367 (7)	350.98 (18)	5.4200 (4)	159.22 (4)		19.80 ± 0.44	33.013 ± 0.10	1.0	1.2

correspond to the PDF number 01-075-7697, indicating the presence of rhombohedral (space group $R\bar{3}c$) for $LaMnO_3$. Sharp and intense diffraction peaks suggest that the $LaMnO_3$ and CeO_2 phases exhibit good crystallinity (Fig. 2(a)). Rietveld refinement was performed (Fig. 2(b)) to determine the composition percentages and lattice parameters, which are summarized in Table 1. Overall, the R_w% for all refinements was less than 2%. The calculated composition ratio matches our initial stoichiometry of the composite.

The Williamson–Hall (W–H) equation $\beta \cos\theta = k\lambda/D + 4\varepsilon \sin\theta$,[18,19] is used to determine the crystallite size (D) from the XRD data. Here, β is the full width at half maximum (in radians) of the peaks, θ is the peak position, k is the Scherrer constant (0.9), λ is the wavelength of the X-ray used, and ε is the lattice strain. The crystallite size is obtained from the Y-intercept of the linear plot of $\beta \cos\theta$ (y-axis) *vs.* $4 \sin\theta$ (x-axis). The W–H equation was plotted using the diffraction peaks at $2\theta = 28.7$, 47.7, and 56.6° for CeO_2 and $2\theta = 22.9$, 32.5, 32.8, 40.2, 46.9, 52.6, 58.2, and 68.1° for $LaMnO_3$. The crystallite size and lattice parameters of LMO and CeO_2 are listed in Table 1. The crystallite size of LMO decreased while CeO_2 increased with increasing CeO_2 content in the composite. The difference in grain growth between LMO and CeO_2 can be attributed to grain boundary migration, which typically occurs through long-range diffusion in a two-phase system with mutually limited solubility.[20] The impediment to grain growth of LMO is evident with the increase in CeO_2 content in the composite.[21] The lattice parameters obtained from the Rietveld analysis of the respective components of the composite are listed in Table 1. The lattice parameters of LMO and CeO_2 remain unaltered across the compositions of the composites. Furthermore, CeO_2, with a cubic structure, and $LaMnO_3$, with a rhombohedral structure, display similar lattice parameters of approximately 5.503 Å. This similarity in lattice parameters reduces the lattice strain at the interface between the two components. With the close lattice matching, the energy cost associated with forming the grain boundary is minimized, thus making it easier for the grains to grow uniformly.

Fig. 3 displays the $LaMnO_3$–CeO_2 composite morphology, elemental map, and spectrum. Fig. 3(a and a′ to e and e′) shows 20 and 5 μm scale FESEM images of LMO, CeO_2, and composite particles. Fig. 3(b and b′) shows a compact and dense morphology of CeO_2 with flake-like or layered structure and granular clusters. The composite morphology becomes more granular with increasing CeO_2 content. The EDX mapping of La (green), Ce (cyan), Mn (blue), and O (red) of $LaMnO_3$–CeO_2 composites is shown in Fig. 3, and the EDX spectrum of synthesized composites is shown in Fig. 3(f–j). The EDX elemental mapping shows a homogeneous coverage of LMO particles with the CeO_2 phase. CeO_2 and $LaMnO_3$, having close lattice "a" parameter (Table 1), could facilitate the growth of CeO_2 over $LaMnO_3$ particles. The lattice match makes the growth of CeO_2 energetically favorable, aligning with the crystal structure of LMO. Consequently, this reduces the strain energy that would otherwise cause CeO_2 to agglomerate as separate particles.

The nitrogen adsorption and desorption isotherms of $LaMnO_3$–CeO_2 composites (Fig. 4) were measured at

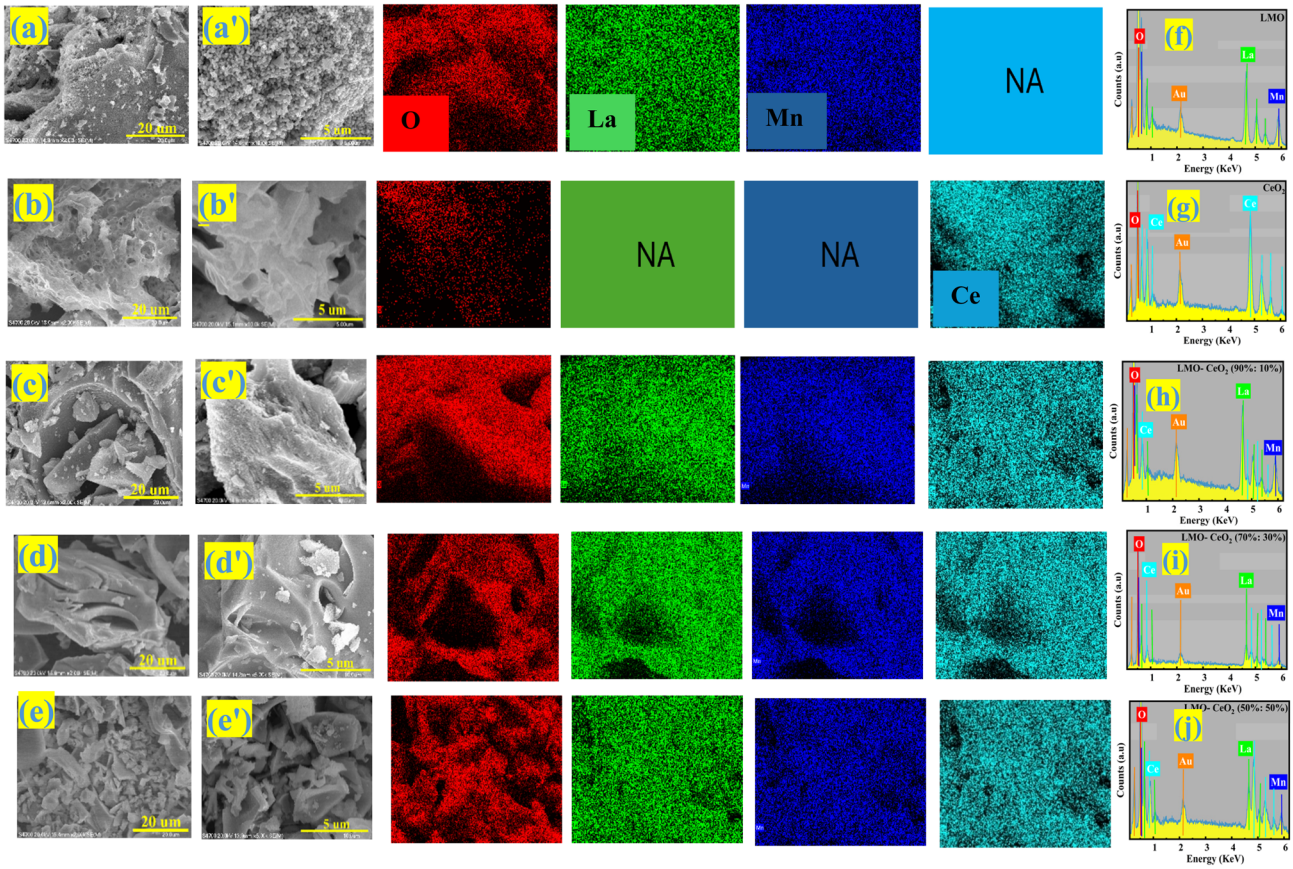

Fig. 3 FESEM images at 20 μm and 5 μm magnifications for (a and a′) LMO, (b and b′) CeO_2, (c and c′) LMO–CeO_2 (90% : 10%), (d and d′) LMO–CeO_2 (70% : 30%), and (e and e′) LMO–CeO_2 (50% : 50%). Elemental mapping of O (red), Mn (blue), La (green), and Ce (cyan color) at 5 μm highlights the distribution of elements in different $LaMnO_3$–CeO_2 composites. (f–j) Corresponding EDX spectra of the $LaMnO_3$–CeO_2 composites. (NA: not applicable.)

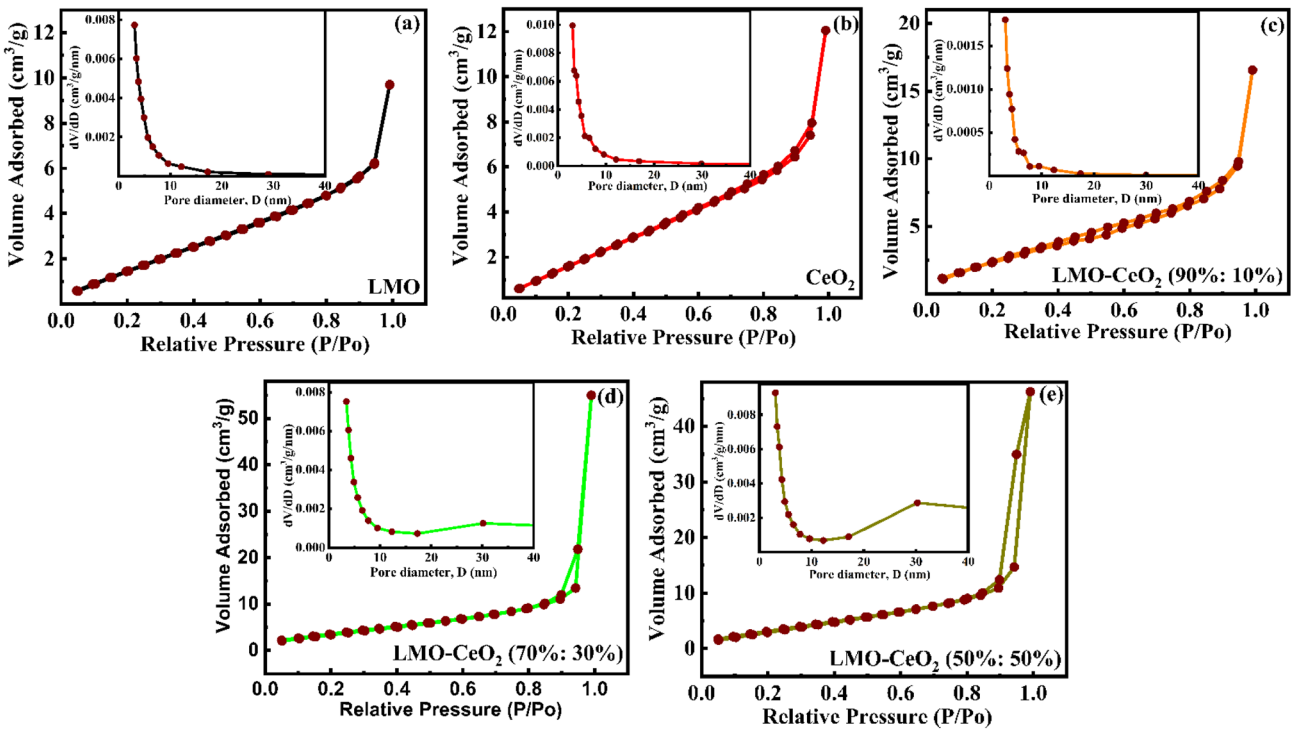

Fig. 4 (a–e) Nitrogen adsorption–desorption isotherms of LMO–CeO_2 composites, with corresponding BJH pore size distribution curves shown in the inset.

Table 2 Surface area and pore size derived from N_2 adsorption and desorption measurement of $LaMnO_3$–CeO_2 composites at 77 K

Composite (LMO–CeO_2)	BET surface area ($m^2\ g^{-1}$)	Average pore size (radius, nm)	Total pore volume ($cc\ g^{-1}$)
LMO	7.70	3.91	0.02
CeO_2	8.86	4.22	0.02
LMO–CeO_2 (90% : 10%)	10.35	5.00	0.03
LMO–CeO_2 (70% : 30%)	14.32	11.91	0.09
LMO–CeO_2 (50% : 50%)	13.54	10.60	0.07

a temperature of 77 K using N_2 gas. The isotherm profile of $LaMnO_3$–CeO_2 composites corresponds to a type IV isotherm with mesoporous characteristics.[22] The pore size distribution and specific surface area were calculated from the desorption data by using the BJH and BET models, respectively, and are listed in Table 2. The LMO–CeO_2 (70% : 30%) composite has the highest specific surface area of 14.32 $m^2\ g^{-1}$, along with a total pore volume of 0.09 $cm^3\ g^{-1}$ and a pore radius of 11.91 nm. Fig. 4 inset shows the BJH pore size distribution. The differential pore volume (d*V*/d*D*) at each pore size indicates the volume available in pores of a given size range. The increase in the d*V*/d*D* value below 10 nm in all samples shows the presence of mesopores (2–50 nm) and micropores (<2 nm) in the material. The porous structure, larger surface area, and pore volume of the composite are beneficial to improving the electrochemical performance of the composite.[23]

The composition and the oxidation states of $LaMnO_3$–CeO_2 composites were analyzed using XPS. The high-resolution spectra of La (Fig. 5(a)) exhibit binding energies at 834.4 and 838 eV for La $3d_{5/2}$ and 850.8 and 855.4 eV for La $3d_{3/2}$, respectively, corresponding to the +3-oxidation state. This implies that La ions are in the trivalent state (La^{3+}), consistent with previously reported values.[24] Fig. 5(b) presents the high-resolution spectra for Mn, displaying two peaks at 641.8 and 653.4 eV for Mn $2p_{3/2}$ and Mn $2p_{1/2}$, respectively. The deconvoluted Mn $2p_{3/2}$ peaks reveal three oxidation states at 640.7,

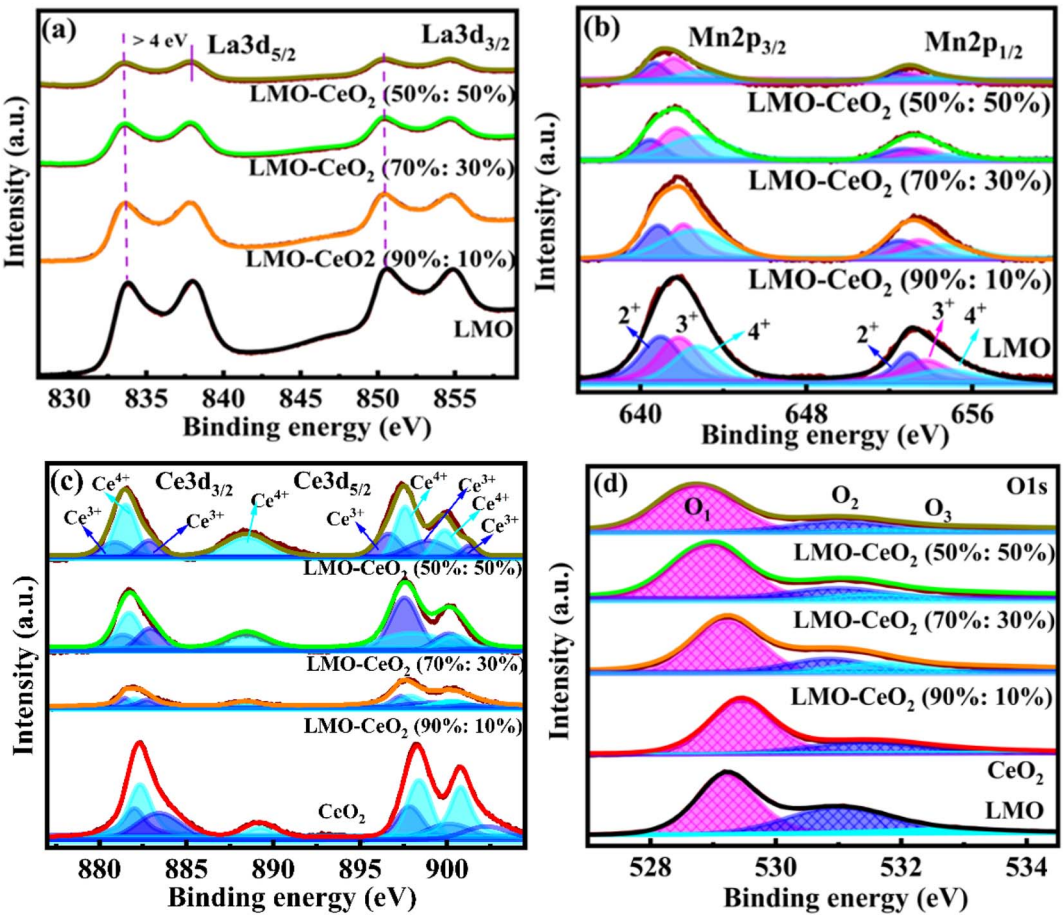

Fig. 5 (a) High-resolution spectrum of La $3d_{5/2}$, (b) high-resolution spectrum of Mn $2p_{1/2}$, (c) high-resolution spectrum of Ce $3d_{5/2}$, and (d) high-resolution spectrum of O 1s.

641.6, and 642.9 eV, which correspond to Mn^{2+}, Mn^{3+}, and Mn^{4+}. Similarly, the deconvoluted Mn $2p_{3/2}$ peaks at 652.4, 653.2, and 654.4 eV corresponds to Mn^{2+}, Mn^{3+}, and Mn^{4+}, respectively.[25] The 882.8, 888.8, 898.2, and 901.2 eV peaks correspond to the Ce^{4+} oxidation state.[26] Additionally, the peaks at 881.1, 885.5, 899.0, and 903.9 eV binding energy confirm the Ce^{3+} oxidation state (Fig. 5(c)).[27] The localization of the electrons left behind in the Ce 4f states due to oxygen defects could lead to the formation of Ce^{3+} ions.[14,28] The coexistence of Ce^{3+} and Ce^{4+} oxidation states verified the incorporation of CeO_2 in the composite. The high-resolution O 1s spectrum of the $LaMnO_3$–CeO_2 composites, illustrated in Fig. 5(d), was deconvoluted into three primary peaks. The first peak (O_1) at 529.4 eV corresponds to lattice oxygen (O_{latt}) present on the surface. The second peak (O_2), appearing at 531.1 eV, is linked to oxygen vacancies or under-coordinated sites (O_{ads}).[13] The third component (O_3), located at 532.8 eV, is attributed to hydroxyl groups arising from adsorbed moisture or surface-bound water molecules.[13,29] The ratios of Mn^{2+}/Mn^{3+} are 0.93, 0.81, 0.70, and 0.69, and Mn^{4+}/Mn^{3+} are 0.98, 1.04, 1.12, and 0.71 for LMO, LMO–CeO_2 (90% : 10%), LMO–CeO_2 (70% : 30%), and LMO–CeO_2 (50% : 50%), respectively. For Ce ions, the ratio of Ce^{3+}/Ce^{4+} is 0.79, 0.98, 1.03, and 0.57 for CeO_2, LMO–CeO_2 (90% : 10%), LMO–CeO_2 (70% : 30%), and LMO–CeO_2 (50% : 50%), respectively. The presence of Mn^{2+}, Mn^{4+}, and Ce^{4+} ions indicates the presence of oxygen deficiency in the corresponding compounds in the composite. A large number of defects are observed in LMO and CeO_2 for the 70% : 30% composite. The presence of oxygen defects enhances the electrochemical properties of $LaMnO_3$–CeO_2 composites.[30] Oxygen vacancies act as active sites for faradaic charge storage in both $LaMnO_3$ and CeO_2, improving the C_{SP} by enhancing the ability of these materials to undergo redox reactions during supercapacitor operation.[23,31]

Electrochemical performance

Cyclic voltammetry (CV). The CV curves of $LaMnO_3$–CeO_2 composites at 10 mV s^{-1} are shown in Fig. 6(a). The area enclosed by the LMO–CeO_2 (70% : 30%) composites is higher than that of others, indicating that the C_{SP} is expected to be higher for these composites. Fig. 6(b–f) shows the CV curves of $LaMnO_3$–CeO_2 composites at different scan rates of 1 to 300 mV s^{-1}. The redox peak can still be observed at 300 mV s^{-1}, indicating that the charge storage mechanism of the electrode is due to the reversible conversions of redox reactions between Ce^{4+} and Ce^{3+} in CeO_2 and Mn^{3+} and Mn^{4+} for $LaMnO_3$ electrodes. Moreover, the oxidation peaks shifted to higher potentials, and the reduction peaks shifted to lower potentials as the scan rates increased. The redox reaction is more kinetically controlled at higher scan rates than purely diffusion-controlled. At higher scan rates, the redox reaction does not occur instantly upon reaching its standard potential because the electrode and electrolyte need time for charge transfer and mass transport to catch up. The reaction becomes kinetically hindered, meaning that additional energy (a more negative reduction potential) is necessary to drive the process at the required rate. The reduction peaks further shifted to lower potentials in LMO–CeO_2 (50% : 50%) composites, which could be attributed to decreased reversibility in the redox processes. This behavior likely arises due to excess CeO_2 disrupting the conductive network within

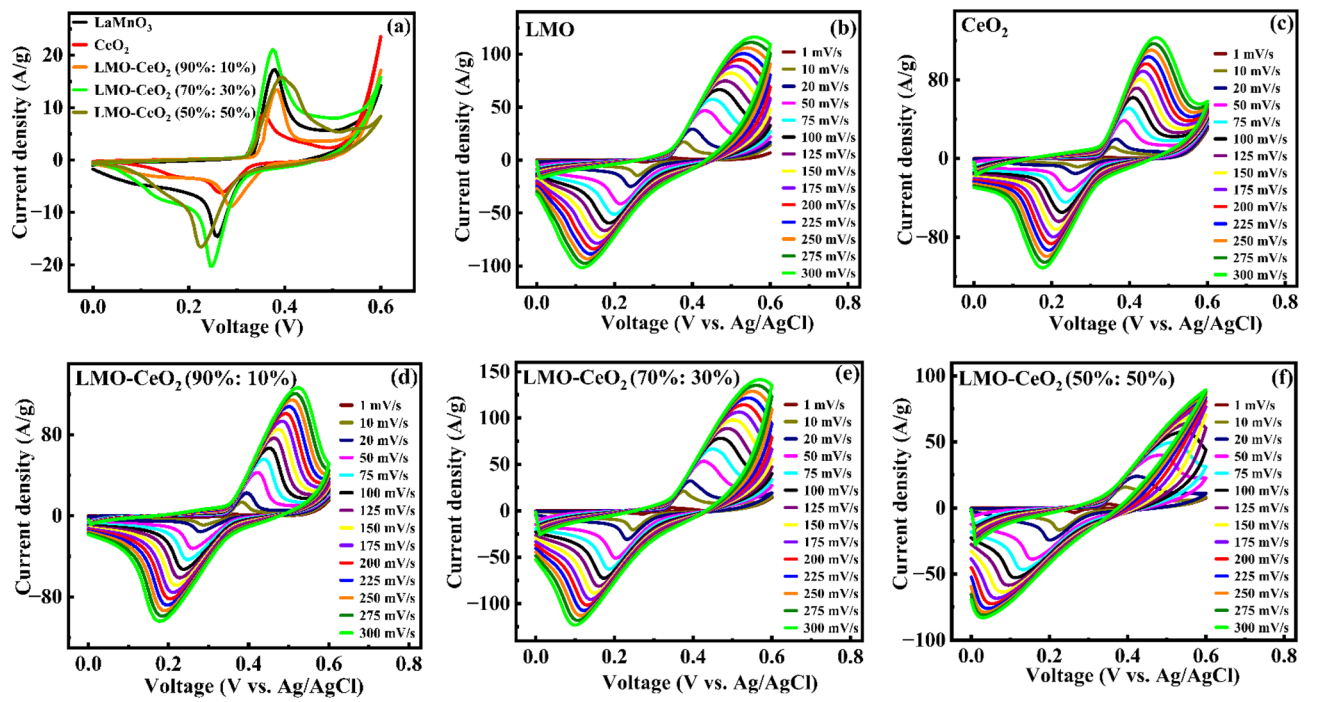

Fig. 6 Cyclic voltammetry measurements of $LaMnO_3$–CeO_2 composites: (a) at a scan rate of 10 mV s^{-1} and (b–f) at different scan rates of 1 to 300 mV s^{-1}.

the composites, blocking an active redox site of LMO, obstructing ion transport pathways, and decreasing the intrinsic reversibility of the $Ce^{3+} \leftrightarrow Ce^{4+}$ redox transition.[32] Concomitantly, a voltage corresponding to the reduction drifts to a lower potential with an increase in CeO_2 content, primarily due to an increase in the overpotential required for reduction. The corresponding adsorption/desorption of OH^- ions from the CeO_2 and $LaMnO_3$ surface can be expressed as eqn (2)–(5):[33,34]

$$Ce^{4+}O_2 + H_2O + e^- \rightarrow Ce^{3+}O{\cdot}OH + OH^- \quad (2)$$

$$Ce^{3+}OOH + OH^- \rightarrow Ce^{4+}O_2 + H_2O + e^- \quad (3)$$

$$La[Mn_{2\delta}{}^{2+};Mn_{(1-2\delta)}{}^{3+}]O_{3-\delta} + 2\delta OH^- \leftrightarrow LaMn^{3+}O_3 + 2\delta e^- + \delta H_2O \quad (4)$$

$$LaMn^{3+}O_3 + 2\delta OH^- \leftrightarrow La[Mn_{2\delta}{}^{4+};Mn_{(1-2\delta)}{}^{3+}]O_{3+\delta} + 2\delta e^- + \delta H_2O \quad (5)$$

Pseudocapacitive materials such as $LaMnO_3$–CeO_2 composites are capable of storing charge in two different mechanisms: (1) through the faradaic electron transfer, which involves the reversible redox reactions of metal ions with their corresponding oxides (*e.g.* Mn(II), Mn(III), and Mn(IV), and Ce(II), and Ce(III)), and (2) *via* non-faradaic charge storage in the electrical double layer on the electrode's surface. Accordingly, the charge–discharge behavior was qualitatively assessed using eqn (6) or (7).[35]

$$i = a\nu^b \quad (6)$$

or

$$\log(i) = \log(a) + b\log(\nu) \quad (7)$$

where a and b are the constants, while i denotes the current density and ν represents the scan rate of the CV measurement. In general, two limiting values exist for b: $b = 0.5$, where the electrochemical behavior is dominated by diffusion-controlled or battery-type processes, slowing the reaction kinetics. On the other hand, $b = 1$ is applied to surface-controlled or electric double-layer capacitance, and the reaction kinetics are fast. When the b values fall between 0.5 and 1, the energy storage kinetics are governed by a combination of both diffusion and surface-controlled reactions. In our work, as shown in Fig. 7(a), the calculated values of b range from 0.53 to 0.65 for the $LaMnO_3$–CeO_2 composites. The b-value of LMO, CeO_2, LMO–CeO_2 (90% : 10%), LMO–CeO_2 (70% : 30%), and LMO–CeO_2 (50% : 50%) composites are calculated to be 0.54, 0.65, 0.62, 0.53, and 0.54, respectively. Furthermore, to evaluate the quantitative contributions to the overall energy storage of the $LaMnO_3$–CeO_2 composites, Dunn's method was applied to distinguish between surface-controlled capacitive effects and diffusion-limited processes, as described by eqn (8) or (9).[36–38]

$$i(V) = k_1\nu + k_2\nu^{1/2} \quad (8)$$

or

$$\frac{i(V)}{\nu^{1/2}} = k_1\nu^{1/2} + k_2 \quad (9)$$

In these equations, $i(V)$ denotes the peak current as a function of scan rate (ν), with k_1 (slope) and k_2 (Y-intercept) are both constant terms.[38] Here, $k_1\nu$ and $k_2\nu^{1/2}$ correspond to current contributions from surface-controlled capacitive processes and diffusion-limited mechanisms, respectively.[36] As illustrated in Fig. 7(b), the diffusion-controlled capacitance contributions at 300 mV s^{-1} are approximately 71, 53, 62, 85, and 81% for LMO, CeO_2, LMO–CeO_2 (90% : 10%), LMO–CeO_2 (70% : 30%), and LMO–CeO_2 (50% : 50%) composites, respectively. However, it is noticed that the diffusion-controlled process persists even at 300 mV s^{-1}, indicating a Faraday-controlled type of redox reaction.

The Randles–Sevcik equation describes the effect of scan rate (ν, mV s^{-1}) on peak current (i_p) for a reversible cyclic voltammogram, representing a diffusion-controlled process (eqn (10)):[39]

$$i_p = 2.69 \times 10^5 AC_0(n^3D\nu)^{1/2} \quad (10)$$

Here, i_p is directly influenced by several parameters, including the electrode area (A, cm^2), the electroactive material's concentration (C_0, mol cm^{-3}), the number of electrons

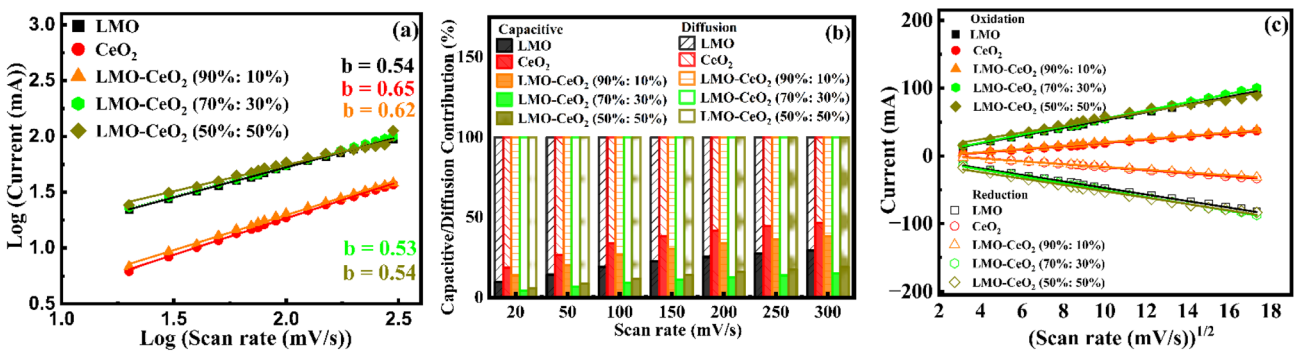

Fig. 7 (a) Relationship between the logarithm of cathodic peak current and the logarithm of scan rates, (b) contribution of capacitive/diffusion-controlled processes at different scan rates, and (c) correlation between peak current from CV curves and the square root of the scan rate of $LaMnO_3$–CeO_2 composites.

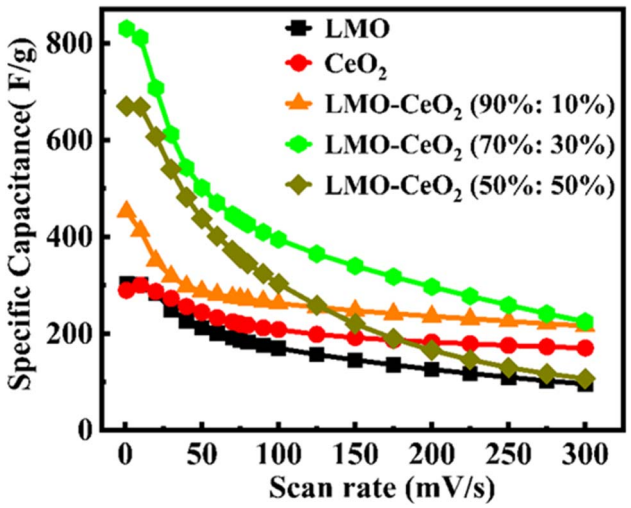

Fig. 8 C_{SP} of $LaMnO_3$–CeO_2 composites at different scan rates.

transferred per molecule (n), the diffusion coefficient (D, $cm^2\ s^{-1}$), and the scan rate (v, $mV\ s^{-1}$). Fig. 7(c) shows the plot of peak current obtained from the CV curves *versus* the square root of the scan rate, which exhibits a linear trend. This linear dependence indicates that a diffusion-controlled mechanism dominates the charge storage behavior.

Fig. 8 presents the C_{SP} values of the $LaMnO_3$–CeO_2 composites, calculated from the integrated area under the CV curves using eqn (11):[40]

$$C_{SP} = \frac{1}{mv\Delta V}\int_{V_a}^{V_c} I(V)\mathrm{d}V \quad (11)$$

where m denotes the mass of the active material in the electrode, $I(V)$ is the response current, and ΔV is the potential window.[36] Here, the integrated part of eqn (11) gives the area enclosed by the current–potential curve or CV curve, which is directly proportional to the C_{SP} of the material. The C_{SP} values of LMO, CeO_2, LMO–CeO_2 (90% : 10%), LMO–CeO_2 (70% : 30%), and LMO–CeO_2 (50% : 50%) are 304, 289, 453, 830, and 670 F g^{-1} at 1 mV s^{-1}, respectively, and are shown in Table 3.

It has been observed that an increase in scan rate leads to a decrease in the C_{SP} of $LaMnO_3$–CeO_2 composites. At low scan rates, the C_{SP} is high because ions with low kinetic energy and resistance have sufficient time to diffuse into the electrode surface. Conversely, at high scan rates, the increased kinetic energy of ions increases their resistance, reducing the time available for them to interact with the electrode surface and resulting in lower C_{SP} values. Furthermore, it demonstrates that the C_{SP} values increase with the increase in the CeO_2 ratio in LMO. This may be due to the presence of oxygen vacancies, defects, and enhanced interfacial and synergistic effects between the LMO and CeO_2 electrodes. Furthermore, the LMO–CeO_2 (70% : 30%) composites have a higher C_{SP} value than those of other composites, indicating this is the optimal composition of this LMO and CeO_2. However, with a higher ratio of CeO_2 in LMO, the C_{SP} of LMO–CeO_2 (50% : 50%) composites decrease. This may be due to particle agglomeration, which implies that the CeO_2 particles may block the ion flow path, thereby limiting ion diffusion and the availability of electroactive sites.

Chronopotentiometry studies. Fig. 9(a) shows the chronopotentiometry charge/discharge curves of $LaMnO_3$–CeO_2 composite electrodes at a current density of 1 A g^{-1}. In all cases, the nonlinear discharge curves are asymmetric to the corresponding charge curves, indicating supercapacitive behavior. Charge/discharge measurements are also carried out at different current densities, ranging from 1 to 15 A g^{-1}, for $LaMnO_3$–CeO_2 composites (Fig. 9(b–f)). At low current densities, the discharge time is observed to be longer for all composites with a small plateau, indicating the extrinsic pseudocapacitive behavior. Dunn *et al.* introduced the concept of the "extrinsic pseudocapacitor" for materials such as $LiCoO_2$. These materials behave as a battery in the bulk phase, but after size reduction, pseudocapacitive behavior emerges.[41,42]

Eqn (12) can be used to calculate the C_{SP} of working electrodes from the charge–discharge curves.[43]

$$C_{SP} = \frac{I_m \times \Delta t}{\Delta V} \quad (12)$$

where I_m represents the current density, m denotes the mass of the active material, Δt refers to the discharge time, and ΔV indicates the potential window. The calculated C_{SP} is 291, 234, 430, 638, and 514 F g^{-1} at a scan rate of 1 A g^{-1} for LMO, CeO_2, LMO–CeO_2 (90% : 10%), LMO–CeO_2 (70% : 30%), and LMO–CeO_2 (50% : 50%) composites, respectively. The LMO–CeO_2 (70 : 30%) composites have a higher C_{SP}, which is 2.19 times higher than that of LMO and 2.7 times higher than that of CeO_2. This result emphasizes the synergistic effects between the LMO and CeO_2 compounds. Fig. 10(a) shows the relationship between the C_{SP} and current densities from 1–15 A g^{-1}.

Fig. 10(b) represents the Ragone plot for the $LaMnO_3$–CeO_2 composites, demonstrating the correlation between the

Table 3 C_{SP}, energy density, and power density of $LaMnO_3$–CeO_2 composites

	C_{SP} (F g^{-1})			
Composites	1 mV s^{-1}	1 A g^{-1}	Energy density (Wh kg^{-1})	Power density (W kg^{-1})
LMO	303.8	290.7	14.5	354.0
CeO_2	289.2	234.2	11.7	351.4
LMO–CeO_2 (90% : 10%)	452.8	430.2	21.5	351.9
LMO–CeO_2 (70% : 30%)	830.3	637.6	31.9	357.5
LMO–CeO_2 (50% : 50%)	670.0	513.6	25.7	350.5

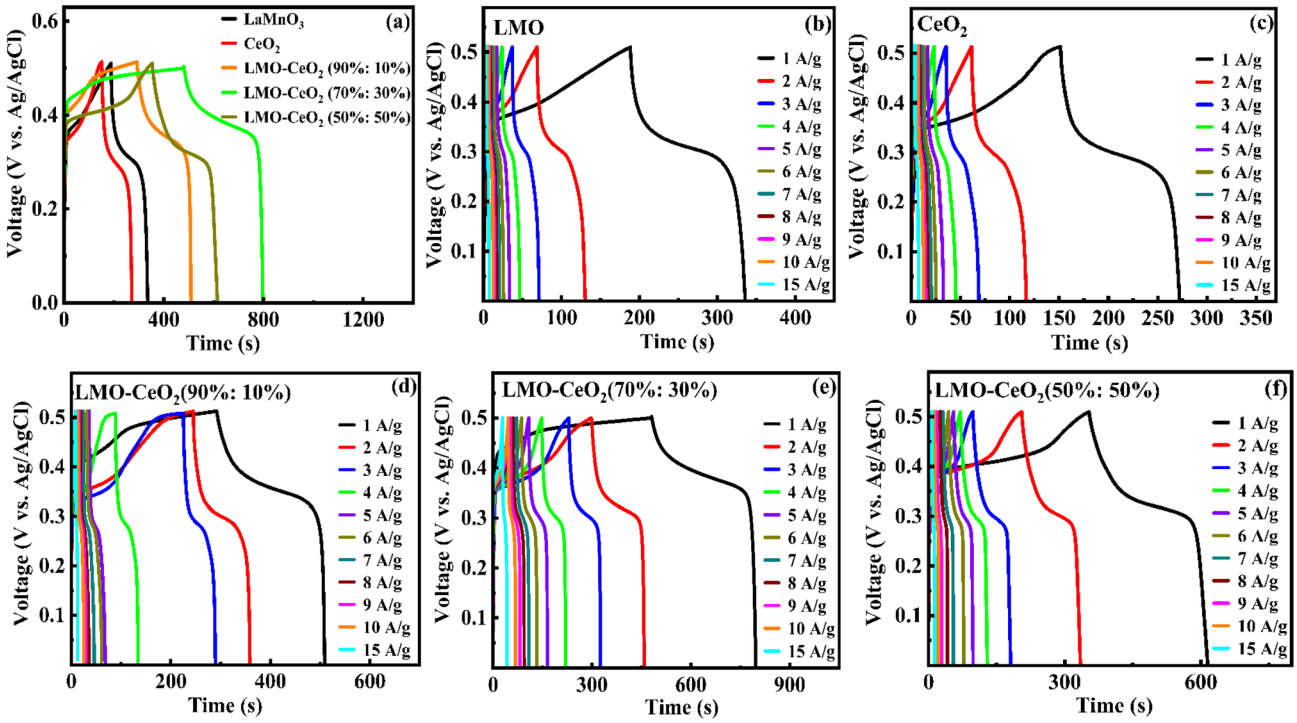

Fig. 9 Charge/discharge curves (a) at a scan rate of 1 A g^{-1} and (b–f) at different current densities from 1 to 15 A g^{-1} for $LaMnO_3$–CeO_2 composites.

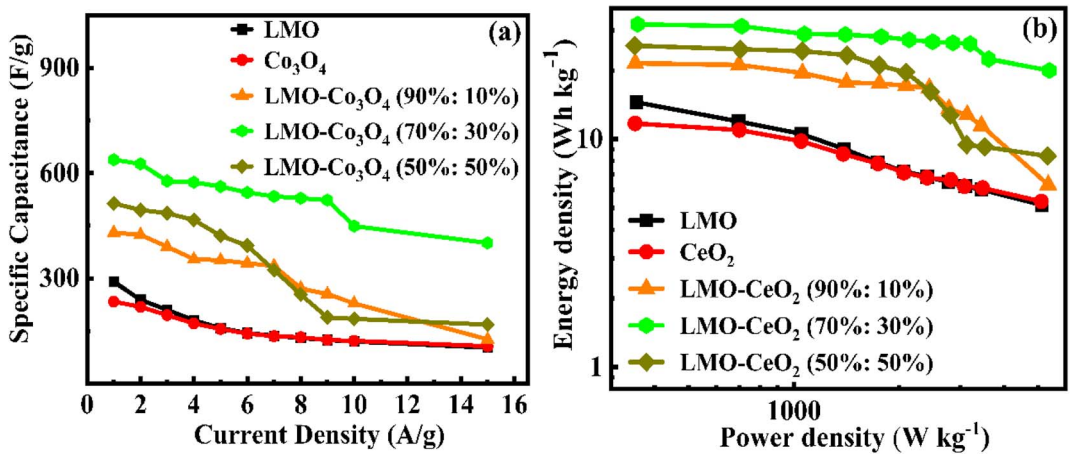

Fig. 10 (a) C_{SP} and (b) Ragone plot of $LaMnO_3$–CeO_2 composites at different current densities.

logarithmic values of energy density and power density. The energy density (E; Wh kg^{-1}) and power density (P; W kg^{-1}) were determined using eqn (13) and (14):[44,45]

$$E = \frac{0.5 \times C_{SP} \times \Delta V^2}{3.6} \quad (13)$$

$$P = \frac{3600 \times E}{\Delta t} \quad (14)$$

where C_{SP} represents specific capacitance (F g^{-1}), and ΔV is the voltage window (V), and Δt is the discharge time (s). The LMO–CeO_2 (70% : 30%) composites have the highest energy density of 31.9 Wh kg^{-1} with a power density of 357.5 W kg^{-1} (Table 3). Even at the high-power density of 5390.8 W kg^{-1}, the energy density is 20.0 Wh kg^{-1}, which is higher than the reported values of CeO_2 compounds.

The ability to maintain capacity over multiple cycles at higher current rates is a crucial requirement for a charge storage device, making it an essential feature of supercapacitors for real-world applications. The cyclic performance for the $LaMnO_3$–CeO_2 composites electrode is depicted in Fig. 11. This was carried out at a constant current density of 10 A g^{-1} using chronopotentiometry charge–discharge cyclic measurement for

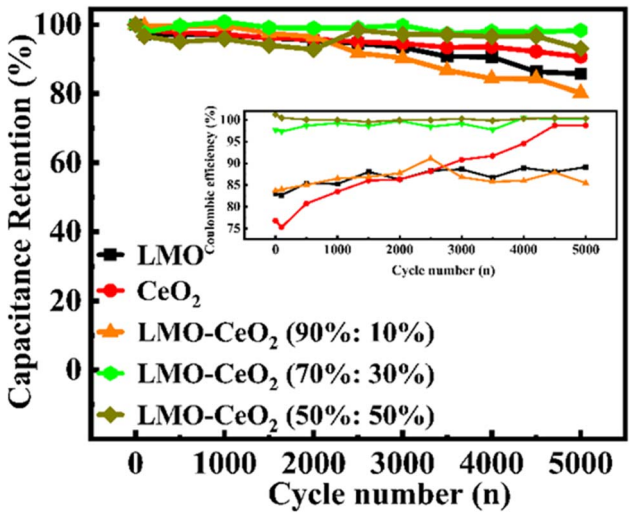

Fig. 11 Cyclic performance and coulombic efficiency (inset) of $LaMnO_3$–CeO_2 composite electrode during 5000 cycles at a current density of 10 A g^{-1}.

5000 continuous cycles. No perceptible degradation was observed in the LMO–CeO_2 (70% : 30%) composite. The capacity retention of LMO–CeO_2 (50% : 50%) composite increases after 2000 cycles, and no degradation is noticed until 4500 cycles. The retention percentages of electrodes prepared using $LaMnO_3$–CeO_2 composites were obtained to be 85.8, 90.7, 80.2, 98.3, and 93.1%, corresponding to a decrease in C_{SP} from 121.0, 122.8, 231.6, 394.2, and 182.3 F g^{-1} to 103.8, 111.4, 185.7, 387.6, and 169.7 F g^{-1} for LMO, CeO_2, LMO–CeO_2 (90% : 10%), LMO–CeO_2 (70% : 30%), and LMO–CeO_2 (50% : 50%) composites, respectively. The higher stability of electrodes of $LaMnO_3$–CeO_2 composites can be attributed to several factors: (i) the structurally integrated composites provide interconnected porous channels that facilitate efficient diffusion of electrolyte ions toward the interior regions, (ii) the close interfacial contact between the $LaMnO_3$–CeO_2 mesoporous core and highly conductive intermediate shell can increase the electrical conductivity of the electrode material, resulting in faster electron transport in the electrode.[46] Additionally, it can effectively adapt to volume variations during faradaic redox reactions across the $LaMnO_3$–CeO_2 core surface, preventing the active electrode material from degradation, thereby ensuring high cycling stability.

The coulombic efficiency as a function of cycle number is shown in the inset of Fig. 11. It specifies the efficacy of converting electrical charge into a useful output during charging and discharging cycles. The coulombic efficiency of electrodes was evaluated using the formula $\eta = (t_D/t_C) \times 100\%$.[47] Where t_D and t_C represent discharging time and charging time, respectively. The result provides the coulombic efficiency of LMO–CeO_2 (70% : 30%) and LMO–CeO_2 (50% : 50%), which exhibit 100% efficiency throughout 5000 cycles at a current density of 10 A g^{-1}. According to these results, the optimal proportion of LMO and CeO_2 composites enhances the electrochemical stability and increases the viability of the redox process.

Table 4 compares the C_{SP}, energy density, and power density of $LaMnO_3$–CeO_2 composites to those of the published articles. It demonstrates that LMO–CeO_2 (70% : 30%) outperforms other composites in terms of C_{SP}, energy, and power density.

Electrochemical impedance spectroscopy (EIS). The impedance spectrum of a supercapacitor is another crucial component to understanding its performance. The primary goal of electrochemical impedance measurements is to analyze the electrode's capacitive and resistive characteristics. The impedance spectra of the $LaMnO_3$–CeO_2 composites are presented in Fig. 12. The Bode diagrams present the relationship between the impedance magnitude ($|z|$) (Fig. 12(a)) and the phase angle between the applied voltage signal and the resulting current (Φ, degrees) (Fig. 12(b)) as a function of AC frequency, while the corresponding Nyquist plots are shown in Fig. 12(c). As depicted in Fig. 12(a), the LMO–CeO_2 (70% : 30%) composite exhibits the lowest impedance values across the high-frequency region, indicating a reduced resistance to ion transport and enhanced electrochemical performance. In the low-frequency region, the phase angle of this composite approaches −80° (Fig. 12(b)),

Table 4 Electrochemical performance metrics of $LaMnO_3$ and CeO_2 based electrode materials for energy storage devices

Material	Current density (A g^{-1})	Electrolyte (KOH)	C_{SP} (F g^{-1})	Energy density, E (Wh kg^{-1})	Power density, P (W kg^{-1})	Ref.
$LaMn_{1\pm x}O_3$	1	1 M	202.1 mAh g^{-1}	—	—	25
$LaMnO_3$–SiO_2	5 mV s^{-1}	1 M	200	—	—	48
$LaMnO_3$–Mn_3O_4 (70% : 30%)	1	6 M	478.8	23.9	355.7	38
CeO_2–Fe_2O_3 nanospindles	5 mV s^{-1}	6 M	142.6	—	—	49
Porous NiO–CeO_2	1	3 M	305	—	—	50
$LaMnO_3$–Co_3O_4 (70% : 30%)	0.5	1 M	660.0	33.0	202.7	45
$LaMnO_3$/rGO/PANI	1	PVA/KOH	802	—	—	51
CeO_2/AC	2 mA cm^{-2}	1 M H_2SO_4	162	—	—	52
Co–CeO_2	2	1 M	573 C g^{-1}	—	—	53
Polythiophene	0.5	Polymer gel	129.13	3	250	54
$La_{0.75}Sr_{0.25}MnO_{3-\delta}/MnO_2$	2 mV s^{-1}	1 M Na_2SO_4	437.2	—	—	55
CeO_2/CeS_2	1	0.1 M	420	21.2	303.0	56
LMO–CeO_2(70% : 30%)	**1**	**1 M**	**637.6**	**31.9**	**357.5**	**Present work**
MnO_2–CeO_2-1	0.5 A g^{-1}	3 M	274.3	—	—	33
$LaMnO_3$/CeO_2	1	1 M Na_2SO_4	262.0	—	—	57

indicating near-ideal capacitive behavior. Although not perfectly capacitive (−90°), the high phase angle signifies rapid charge storage kinetics and efficient charge transport at the electrode–electrolyte interface. In the Nyquist plot of $LaMnO_3$–CeO_2 composites, where Z_{re} (*X*-axis) and Z_{im} (*Y*-axis) are the real and imaginary parts of the impedance, measured in the frequency range from 100 kHz to 0.01 Hz. The insets in Fig. 12(c) are the equivalent circuit, which consists of solution resistance (R_1), open Warburg impedance (W_o), interfacial resistance (R_2), and a constant phase element (CPE). The intersection of the EIS plots and the real axis represent the solution resistance of the electrode (R_1). This can be written as the combination of the contributions from uncompensated contact resistance and the interface.[58] The high-frequency loop corresponds to the charge transfer resistance (R_2) across the catalyst/electrolyte interface.[59] At low frequencies, the linear portion of the Nyquist plot typically represents Warburg impedance, associated with ion diffusion within the electrode and electrolyte. The R_2 value of the LMO–CeO_2 (70% : 30%) composite is the lowest among the composites, indicating the composite's ability for a rapid charge transfer rate, which increases its inherent electronic conductivity and electrochemical activity. The CPE arises from a distribution of time constants, which can be attributed to the variability in R_1 and/or the dispersion of interfacial capacitance.

The impedance of a CPE is expressed by $Z_{CPE} = \frac{1}{Q(j\omega)^{\alpha}}$ where, Q and α are the parameters defining the CPE. In the above expression, Q is expressed in Ω^{-1} s^{a}, and α is the dimensionless parameter that ranges between 0 and 1. When $\alpha = 1$, 0, and 0.5, the system behaves as a pure capacitor, resistance, and Warburg impedance, respectively.[60] The EIS analysis revealed that the R_2 values are 21.21, 28.05, 8.83, 6.83, and 9.25 Ω from LMO, CeO_2, LMO–CeO_2 (90% : 10%), LMO–CeO_2 (70% : 30%), and LMO–CeO_2 (50% : 50%) composites, respectively, indicating that the composites can boost the conductivity of the individual compounds. R_2 is related to the electrode area where the electrolyte ions can access; that is, the power control factor for the supercapacitor.[61] The lower R_2 values of the material further indicate that it had lower resistance and aided in maintaining stability during the electrochemical measurements. The impedance values of $LaMnO_3$–CeO_2 composites were determined by fitting in the "Gamry Echem Analyst" software and are presented in Table 5.

This study observed that increasing the CeO_2 concentrations on LMO by up to 30% enhances the C_{SP}, energy density, and power density. The LMO–CeO_2 (70% : 30%) composite exhibits the highest C_{SP} due to an optimal balance between structure, conductivity, and ion accessibility achieved at this ratio. This composition creates a highly interconnected conducting network that significantly enhances electron transport while reducing interfacial resistance, a crucial factor for the rapid redox reactions required for efficient charge storage. LMO provides excellent supercapacitive behavior in this setup, contributing to the primary capacitance. At the same time, CeO_2 introduces structural stability, oxygen vacancies, and a slight boost in conductivity, supporting both longevity and additional charge storage sites. The LMO–CeO_2 (70% : 30%) composites enable these materials to work synergistically, maximizing their electrochemical strengths. Moreover, the mesoporous structure observed in this composite, with a specific surface area of 14.32 m^2 g^{-1}, facilitates easy access to the electrolyte, allowing for the

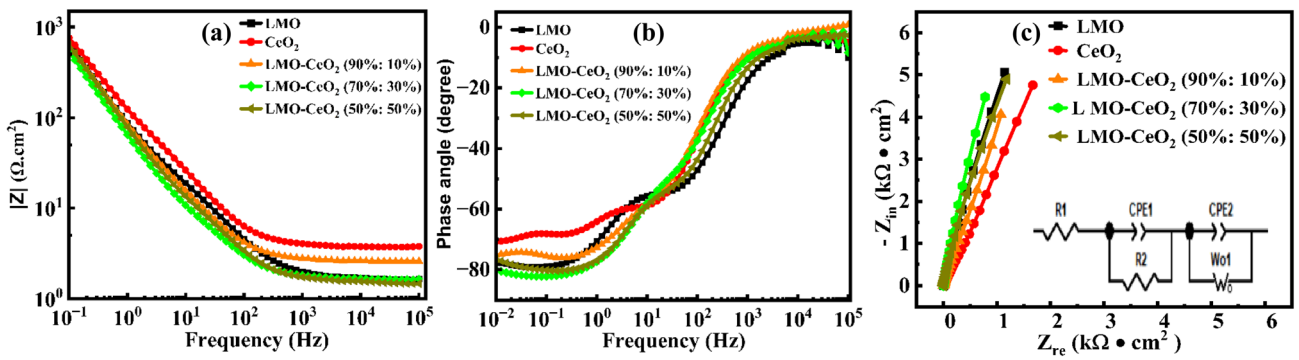

Fig. 12 EIS Bode plots of (a) impedance magnitude and (b) phase change *vs.* AC frequency. Nyquist plot (c) of $LaMnO_3$–CeO_2 composites illustrated with the fitted equivalent circuit (inset figure).

Table 5 Nyquist plot fitting values for $LaMnO_3$–CeO_2 composites

Composites	R_1 (Ω)	R_2 (Ω)	W_o (Ω, $\times 10^{-3}$)	CPE_1 (α)	CPE_1 (Q; Ω^{-1} s^{a})	CPE_2 (α)	CPE_2 (Q; Ω^{-1} s^{a})	Goodness of fit ($\times 10^{-3}$)
LMO	1.619	21.21	0.142	0.711	0.004	0.934	0.002	0.953
CeO_2	3.721	28.05	0.195	0.750	0.004	0.852	0.001	0.646
LMO–CeO_2 (90% : 10%)	2.573	8.830	0.200	0.713	0.008	0.891	0.002	0.176
LMO–CeO_2 (70% : 30%)	1.618	6.831	0.106	0.689	0.008	0.944	0.003	0.703
LMO–CeO_2 (50% : 50%)	1.493	9.253	0.186	0.711	0.006	0.946	0.002	1.364

accommodation of more ions during charge–discharge cycles and thereby increasing the overall capacitance. Ratios with higher CeO_2 content, such as the LMO–CeO_2 (50% : 50%) composite, begin to block ion transport pathways and hinder access to active sites, thereby reducing capacitance. In contrast, a lower CeO_2 content, such as the LMO–CeO_2 (90% : 10%) composition, lacks structural enhancement and additional redox sites provided by CeO_2, resulting in a less efficient charge storage process. Therefore, the LMO–CeO_2 (70% : 30%) composition strikes an ideal balance, offering a high surface area, optimal pore structure, and efficient ion and electron transport, all of which contribute to its superior electrochemical performance.

Conclusion

Crystalline $LaMnO_3$–CeO_2 composites, synthesized through an autocombustion method, exhibit significantly enhanced electrochemical properties driven by synergistic interactions between $LaMnO_3$ (LMO) and CeO_2. The LMO–CeO_2 (70 : 30) composite, characterized by a BET specific surface area of 14.32 $m^2\ g^{-1}$, achieved a superior specific capacitance of 637.6 F g^{-1} at a current density of 1 A g^{-1}, with an energy density of 31.9 Wh kg^{-1} and a power density of 357.5 W kg^{-1}. This enhanced performance is attributed to a robust, interconnected conductive network, reduced contact resistance, and improved electron transport at the electrode–electrolyte interface. However, increasing CeO_2 content beyond 30% led to diminished electrochemical performance, likely due to impeded ion diffusion pathways. These findings highlight the potential of optimized $LaMnO_3$–CeO_2 composites for advanced supercapacitor applications and provide critical insights into tailoring composite ratios to maximize electrochemical efficiency.

Conflicts of interest

The authors confirm that they have no known financial or personal conflicts of interest that could have influenced the work presented in this paper.

Data availability

The data are available in this link: **https://zenodo.org/uploads/17058741**.

Acknowledgements

The authors express their gratitude to the University of Memphis for its support in conducting this research work.

References

1 A. M. Omer, Energy, environment and sustainable development, *Renewable Sustainable Energy Rev.*, 2008, **12**(9), 2265–2300.
2 M. Winter and R. J. Brodd, What are batteries, fuel cells, and supercapacitors?, *Chem. Rev.*, 2004, **104**(10), 4245–4270.
3 C. C. Hu and W. C. Chen, Effects of substrates on the capacitive performance of $RuO_x \cdot nH_2O$ and activated carbon–RuO_x electrodes for supercapacitors, *Electrochim. Acta*, 2004, **49**(21), 3469–3477.
4 B. Y. Guan, A. Kushima, L. Yu, S. Li, J. Li and X. W. Lou, Coordination polymers derived general synthesis of multishelled mixed metal-oxide particles for hybrid supercapacitors, *Adv. Mater.*, 2017, **29**(17), 1605902.
5 C. C. Hu, K. H. Chang, M. C. Lin and Y. T. Wu, Design and tailoring of the nanotubular arrayed architecture of hydrous RuO_2 for next generation supercapacitors, *Nano Lett.*, 2006, **6**(12), 2690–2695.
6 L. He, Z. Luo, P. Liu, X. Zhu, W. Fan, Q. Yu, *et al.*, Fast polysulfides conversion and regulated lithium plating enabled by W_2N quantum dots for high-performance lithium sulfur batteries, *EcoEnergy*, 2025, **3**(1), 192–201.
7 Z. A. Elsiddig, D. Wang, H. Xu, W. Zhang, T. Zhang, P. Zhang, *et al.*, Three-dimensional nitrogen-doped graphene wrapped $LaMnO_3$ nanocomposites as high-performance supercapacitor electrodes, *J. Alloys Compd.*, 2018, **740**, 148–155.
8 D. U. Lee, M. G. Park, H. W. Park, M. H. Seo, V. Ismayilov, R. Ahmed, *et al.*, Highly active Co-doped $LaMnO_3$ perovskite oxide and N-doped carbon nanotube hybrid bi-functional catalyst for rechargeable zinc–air batteries, *Electrochem. Commun.*, 2015, **60**, 38–41.
9 X. Sun, Z. Hao, F. Zeng, J. Xu, H. Nan, Z. Meng, *et al.*, Coaxial cable-like dual conductive channel strategy in polypyrrole coated perovskite lanthanum manganite for high-performance asymmetric supercapacitors, *J. Colloid Interface Sci.*, 2022, **610**, 601–609.
10 A. Arya, S. Tanwar, M. Iqbal, A. Sharma and A. L. Sharma, Synergetic effect driven $LaMnO_3$@NiO composite based high energy semi-solid supercapacitor, *J. Energy Storage*, 2025, **105**, 114778.
11 P. M. Shafi, N. Nisar and A. C. Bose, One-Pot synthesis of $LaMnO_3/Mn_3O_4$ Nanocomposite: Impact of Calcination Temperature on the Synergetic Effect Towards High Energy Supercapacitor Performance, *ChemistrySelect*, 2018, **3**(23), 6459–6467.
12 P. Ma, N. Lei, B. Yu, Y. Liu, G. Jiang, J. Dai, *et al.*, Flexible supercapacitor electrodes based on carbon cloth-supported $LaMnO_3$/MnO nano-arrays by one-step electrodeposition, *Nanomaterials*, 2019, **9**(12), 1676.
13 H. Tian, X. Lang, H. Nan, P. An, W. Zhang, X. Hu, *et al.*, Nanosheet-assembled $LaMnO_3$@$NiCo_2O_4$ nanoarchitecture growth on Ni foam for high power density supercapacitors, *Electrochim. Acta*, 2019, **318**, 651–659.
14 J. Paier, C. Penschke and J. Sauer, Oxygen defects and surface chemistry of ceria: quantum chemical studies compared to experiment, *Chem. Rev.*, 2013, **113**(6), 3949–3985.
15 B. Niu, F. Zhang, H. Ping, N. Li, J. Zhou, L. Lei, *et al.*, Sol-gel autocombustion synthesis of nanocrystalline high-entropy alloys, *Sci. Rep.*, 2017, **7**(1), 3421.
16 D. Bokov, A. Turki Jalil, S. Chupradit, W. Suksatan, M. Javed Ansari, I. H. Shewael, *et al.*, Nanomaterial by sol-gel method:

synthesis and application, *Adv. Mater. Sci. Eng.*, 2021, **2021**(1), 5102014.
17 A. Dhakal, F. Perez and S. R. Mishra, Urea-driven hydrothermal synthesis of Mn_2O_3: electrochemical performance across various electrolytes for supercapacitor applications, *Energy Adv.*, 2025, **4**, 878–895.
18 S. B. Narang and K. Pubby, Nickel spinel ferrites: a review, *J. Magn. Magn. Mater.*, 2021, **519**, 167163.
19 A. Dhakal, F. A. Perez and S. R. Mishra, Electrochemical assessment of tailored Mn_2O_3 cuboidal hierarchical particles prepared using urea and Piperazine, *Electrochim. Acta*, 2024, **507**, 145169.
20 D. Fan and L. Q. Chen, Topological evolution during coupled grain growth and Ostwald ripening in volume-conserved 2-D two-phase polycrystals, *Acta Mater.*, 1997, **45**(10), 4145–4154.
21 D. Das, C. M. Srivastava, D. Bahadur, A. K. Nigam and S. K. Malik, Magnetic and electrical transport properties of $La_{0.67}Ca_{0.33}MnO_3$ (LCMO):xZnO composites, *J. Phys.: Condens. Matter*, 2004, **16**(23), 4089.
22 R. Bardestani, G. S. Patience and S. Kaliaguine, Experimental methods in chemical engineering: specific surface area and pore size distribution measurements—BET, BJH, and DFT, *Can. J. Chem. Eng.*, 2019, **97**(11), 2781–2791.
23 G. R. Li, Z. P. Feng, Y. N. Ou, D. Wu, R. Fu and Y. X. Tong, Mesoporous MnO_2/carbon aerogel composites as promising electrode materials for high-performance supercapacitors, *Langmuir*, 2010, **26**(4), 2209–2213.
24 M. F. Sunding, K. Hadidi, S. Diplas, O. M. Løvvik, T. E. Norby and A. E. Gunnæs, XPS characterisation of in situ treated lanthanum oxide and hydroxide using tailored charge referencing and peak fitting procedures, *J. Electron Spectrosc. Relat. Phenom.*, 2011, **184**(7), 399–409.
25 Z. A. Elsiddig, H. Xu, D. Wang, W. Zhang, X. Guo, Y. Zhang, *et al.*, Modulating Mn^{4+} ions and oxygen vacancies in nonstoichiometric $LaMnO_3$ perovskite by a facile sol-gel method as high-performance supercapacitor electrodes, *Electrochim. Acta*, 2017, **253**, 422–429.
26 E. Bêche, P. Charvin, D. Perarnau, S. Abanades and G. Flamant, Ce 3d XPS investigation of cerium oxides and mixed cerium oxide ($Ce_xTi_yO_z$), *Surf. Interface Anal.*, 2008, **40**, 264–267.
27 S. Nagamuthu, S. Vijayakumar and K. S. Ryu, Cerium oxide mixed $LaMnO_3$ nanoparticles as the negative electrode for aqueous asymmetric supercapacitor devices, *Mater. Chem. Phys.*, 2017, **199**, 543–551.
28 H. Y. Li, H. F. Wang, X. Q. Gong, Y. L. Guo, Y. Guo, G. Lu, *et al.*, Multiple configurations of the two excess 4f electrons on defective CeO_2 (111): Origin and implications, *Phys. Rev. B: Condens. Matter Mater. Phys.*, 2009, **79**(19), 193401.
29 C. Zhang, C. Wang, W. Zhan, Y. Guo, Y. Guo, G. Lu, *et al.*, Catalytic oxidation of vinyl chloride emission over $LaMnO_3$ and $LaB_{0.2}Mn_{0.8}O_3$ (B = Co, Ni, Fe) catalysts, *Appl. Catal., B*, 2013, **129**, 509–516.
30 Y. Sun, M. Guo, S. Shu, D. Ding, C. Wang, Y. Zhang, *et al.*, Preparation of Li_2MnO_3 nanowires with structural defects as high rate and high capacity cathodes for lithium-ion batteries, *Appl. Surf. Sci.*, 2022, **585**, 152605.
31 P. M. Shafi, D. Mohapatra, V. P. Reddy, G. Dhakal, D. R. Kumar, D. Tuma, *et al.*, Sr- and Fe-substituted $LaMnO_3$ Perovskite: Fundamental insight and possible use in asymmetric hybrid supercapacitor, *Energy Storage Mater.*, 2022, **45**, 119–129.
32 H. Angerstein-Kozlowska, B. E. Conway and W. B. A. Sharp, The real condition of electrochemically oxidized platinum surfaces: Part I. Resolution of component processes, *J. Electroanal. Chem. Interfacial Electrochem.*, 1973, **43**(1), 9–36.
33 H. Zhang, J. Gu, J. Tong, Y. Hu, B. Guan, B. Hu, *et al.*, Hierarchical porous MnO_2/CeO_2 with high performance for supercapacitor electrodes, *Chem. Eng. J.*, 2016, **286**, 139–149.
34 H.-s. Nan, X.-y. Hu and H.-w. Tian, Recent advances in perovskite oxides for anion-intercalation supercapacitor: a review, *Mater. Sci. Semicond. Process.*, 2019, **94**, 35–50.
35 J. Liu, J. Wang, C. Xu, H. Jiang, C. Li, L. Zhang, *et al.*, Advanced energy storage devices: basic principles, analytical methods, and rational materials design, *Adv. Sci.*, 2018, **5**(1), 1700322.
36 Y. J. Cao, C. Y. Lu, Z. W. Zhang, Z. Wang, Y. H. Kang, T. T. Yang, *et al.*, N/O co-doped porous carbons derived from coal tar pitch for ultra-high specific capacitance supercapacitors, *ACS Omega*, 2022, **7**(27), 23342–23352.
37 T. Liu, W. G. Pell, B. E. Conway and S. L. Roberson, Behavior of molybdenum nitrides as materials for electrochemical capacitors: comparison with ruthenium oxide, *J. Electrochem. Soc.*, 1998, **145**(6), 1882.
38 A. Dhakal, F. A. Perez, S. Karna and S. R. Mishra, $LaMnO_3$-Mn_3O_4 nanocomposite: Synergetic effect towards high electrochemical performance, *J. Alloys Compd.*, 2024, **1008**, 176262.
39 R. S. Nicholson, Theory and application of cyclic voltammetry for measurement of electrode reaction kinetics, *Anal. Chem.*, 1965, **37**(11), 1351–1355.
40 B. E. Conway, *Electrochemical Supercapacitors: Scientific Fundamentals and Technological Applications*, Springer Science & Business Media, 2013.
41 V. Augustyn, P. Simon and B. Dunn, Pseudocapacitive oxide materials for high-rate electrochemical energy storage, *Energy Environ. Sci.*, 2014, **7**(5), 1597–1614.
42 Y. Jiang and J. Liu, Definitions of pseudocapacitive materials: a brief review, *Energy Environ. Mater.*, 2019, **2**(1), 30–37.
43 Y. Wang, Y. Song and Y. Xia, Electrochemical capacitors: mechanism, materials, systems, characterization and applications, *Chem. Soc. Rev.*, 2016, **45**(21), 5925–5950.
44 A. J. Bard, L. R. Faulkner and H. S. White, *Electrochemical Methods: Fundamentals and Applications*, John Wiley & Sons, 2022.
45 A. Dhakal, F. A. Perez and S. R. Mishra, Synergetic effect towards high electrochemical performance in $LaMnO_3$-Co_3O_4 composites, *Energy Adv.*, 2025, **4**, 162–175.
46 S. Kandula, K. R. Shrestha, N. H. Kim and J. H. Lee, Fabrication of a 3D hierarchical sandwich Co_9S_8/α-MnS@N–C@MoS_2 nanowire architectures as advanced

electrode material for high performance hybrid supercapacitors, *Small*, 2018, **14**, 1800291.

47 B. D. Adams, J. Zheng, X. Ren, W. Xu and J. Zhang, Accurate determination of coulombic efficiency for lithium metal anodes and lithium metal batteries, *Adv. Energy Mater.*, 2018, **8**(7), 1702097.

48 G. W. Piburn, J. T. Mefford, N. Zinni, K. J. Stevenson and S. M. Humphrey, Synthesis and charge storage properties of templated $LaMnO_3$–SiO_2 composite materials, *Dalton Trans.*, 2017, **46**, 977–984.

49 N. S. Arul, D. Mangalaraj, R. Ramachandran, A. N. Grace and J. I. Han, Fabrication of CeO_2/Fe_2O_3 composite nanospindles for enhanced visible light driven photocatalysts and supercapacitor electrodes, *J. Mater. Chem. A*, 2015, **3**, 15248–15258.

50 N. Padmanathan and S. Selladurai, Electrochemical capacitance of porous NiO–CeO_2 binary oxide synthesized via sol–gel technique for supercapacitor, *Ionics*, 2014, **20**, 409–420.

51 P. M. Shafi, V. Ganesh and A. C. Bose, $LaMnO_3$/RGO/PANI ternary nanocomposites for supercapacitor electrode application and their outstanding performance in all-solid-state asymmetrical device design, *ACS Appl. Energy Mater.*, 2018, **1**, 2802–2812.

52 L. S. Aravinda, K. U. Bhat and B. R. Bhat, Nano CeO_2/activated carbon based composite electrodes for high performance supercapacitor, *Mater. Lett.*, 2013, **112**, 158–161.

53 R. Murugan, G. Ravi, R. Yuvakkumar, S. Rajendran, N. Maheswari, G. Muralidharan, *et al.*, Pure and Co doped CeO_2 nanostructure electrodes with enhanced electrochemical performance for energy storage applications, *Ceram. Int.*, 2017, **43**, 10494–10501.

54 N. Mahato, S. Singh, T. V. M. Sreekanth, K. Yoo and J. Kim, In-situ engineered highly crystalline polythiophene empowered electrochemical capacitor-I: Synthesis, characterization, and electrochemical charge storage, *Mater. Lett.*, 2024, **365**, 136483.

55 J. Lv, Y. Zhang, Z. Lv, X. Huang, Z. Wang, X. Zhu, *et al.*, Strontium doped lanthanum manganite/manganese dioxide composite electrode for supercapacitor with enhanced rate capability, *Electrochim. Acta*, 2016, **222**, 1585–1591.

56 N. Bibi, Y. Xia, S. Ahmed, Y. Zhu, S. Zhang and A. Iqbal, Highly stable mesoporous CeO_2/CeS_2 nanocomposite as electrode material with improved supercapacitor electrochemical performance, *Ceram. Int.*, 2018, **44**, 22262–22270.

57 Y. Cao, J. Liang, X. Li, L. Yue, Q. Liu, S. Lu, *et al.*, Recent advances in perovskite oxides as electrode materials for supercapacitors, *Chem. Commun.*, 2021, **57**, 2343–2355.

58 M. Ciureanu and R. Roberge, Electrochemical impedance study of PEM fuel cells. Experimental diagnostics and modeling of air cathodes, *J. Phys. Chem. B*, 2001, **105**, 3531–3539.

59 H. S. Magar, R. Y. Hassan and A. Mulchandani, Electrochemical impedance spectroscopy (EIS): Principles, construction, and biosensing applications, *Sensors*, 2021, **21**, 6578.

60 J. B. Jorcin, M. E. Orazem, N. Pébère and B. Tribollet, CPE analysis by local electrochemical impedance spectroscopy, *Electrochim. Acta*, 2006, **51**, 1473–1479.

61 B. Saravanakumar, K. K. Purushothaman and G. Muralidharan, Interconnected V_2O_5 nanoporous network for high-performance supercapacitors, *ACS Appl. Mater. Interfaces*, 2012, **4**, 4484–4490.